

# I2I-Mamba: Multi-modal medical image synthesis via selective state space modeling

Omer F. Atli, Bilal Kabas, Fuat Arslan, Arda C. Demirtas, Mahmut Yurt, Onat Dalmaz, and Tolga Çukur\*

**Abstract**—In recent years, deep-learning models based on advanced network architectures have helped push the performance envelope in synthesizing unacquired target modalities from acquired source modalities. As this challenging task involves nonlinear transformation of tissue signals that exhibit interactions across varying spatial distances, the utility of an architecture in multi-modal synthesis depends on its ability to express the resultant contextual features. Convolutional neural networks (CNNs) based on compact filters offer high local precision at the expense of poor sensitivity to long-range context. While transformers based on attention-driven filters enhance long-range sensitivity, they suffer from an unfavorable trade-off between sensitivity to long- versus short-range context due to intrinsic model complexity. Here, we propose a novel method for multi-modal medical image synthesis, I2I-Mamba, that leverages selective state space modeling (SSM) to efficiently capture long-range context while maintaining high local precision. To do this, I2I-Mamba episodically injects channel-mixed Mamba (cmMamba) blocks in the bottleneck of a convolutional backbone. Unlike conventional SSM modules, cmMamba blocks are equipped with a novel spiral-scan trajectory to learn context with isotropic spatial footprint across feature maps, and with channel-mixing layers to aggregate context across the channel dimension. Comprehensive demonstrations are reported for imputing missing images in multi-contrast MRI and MRI-CT protocols. Our results indicate that I2I-Mamba offers superior performance against state-of-the-art methods in synthesizing target-modality images.

**Index Terms**—medical image synthesis, modality, imputation, context, state space, Mamba

## I. INTRODUCTION

Multi-modal medical images with distinct tissue contrasts provide complementary information about underlying anatomy, boosting performance and reliability in downstream analyses [1]. Multi-modal imaging is viable using different sequences on the same scanner or on entirely different scanners, albeit costs of running prolonged exams yield incomplete protocols under many clinical scenarios [2]. As a remedy, target-modality images missing from a protocol can be synthesized based on the subset of source-modality images available [3], [4]. Such synthesis tasks involve nonlinear transformation of

This study was supported by TUBA GEBIP 2015 and BAGEP 2017 fellowships awarded to T. Çukur (Corresponding author: Tolga Çukur, cukur@ee.bilkent.edu.tr).

O.F. Atli, B. Kabas, F. Arslan, A.C. Demirtas and T. Çukur are with the Department of Electrical and Electronics Engineering, Bilkent University, Ankara, Turkey (e-mails: {faruk.atli, bilal.kabas, fuat.arslan, cinar.demirtas}@bilkent.edu.tr). T. Çukur is also with the National Magnetic Resonance Research Center (UMRAM), and the Department of Neuroscience, Bilkent University, TR-06800 Ankara, Turkey.

O. Dalmaz and M. Yurt are with the Department of Electrical Engineering, Stanford University, CA 94305, United States (e-mails: {onat, myurt}@stanford.edu).

signal levels between source and target images depending on tissue characteristics [5]. Although detailed tissue parameters that govern signal levels are generally difficult to infer from medical images, multi-modal synthesis can be guided via a rudimentary spatial prior on tissue composition that can be implicitly inferred from the signal distribution in source images [6]. Note that both healthy and pathological tissues can exhibit broad spatial distribution in the form of contiguous or segregated clusters across an anatomy [7], introducing not only local signal correlations in compact neighborhoods but also non-local signal correlations over extended distances. Thus, successful solution of a multi-modal synthesis task inherently rests on the ability to capture these short- and long-range contextual features in medical images.

Deep learning has recently emerged as the mainstream framework for medical image synthesis given its prowess in nonlinear function approximation [8]–[11]. In learning-based synthesis, a neural network model attempts to map source onto target images through hierarchical nonlinear transformations on intermediate feature maps [12], [13]. Naturally, the fidelity of this mapping depends on the model’s expressiveness for the diverse set of contextual features in medical images. Earlier studies have used CNN-based models with convolution operators for local filtering of feature maps [13]–[16]. The popularity of CNNs has been fueled by linear model complexity with respect to image dimensionality, and high expressiveness for local context that can be critical in synthesis of detailed tissue structure [17]–[27]. However, convolution operators have strictly localized spatial footprints, inducing poor sensitivity to long-range contextual features [28], [29]. In turn, CNNs can suffer from low synthesis accuracy near regions of heterogeneous tissue composition and uncommon pathology, where contextual relations often serve a key role in inferring the spatial distribution of tissue signals [30], [31].

Later studies have instead adopted transformer-based models based on self-attention operators that are capable of non-local filtering [28], [32]–[34]. Tokenizing an input image as a sequence of patches, transformers compute attention weights to measure inter-patch similarity and use these weights to non-locally filter the input sequence. While the diffuse spatial footprints of self-attention operators help increase sensitivity to long-range context, they induce quadratic model complexity with respect to sequence length (i.e., number of image patches), which can prohibit their use on small patches necessary to maintain high spatial precision, and compromise their learning efficiency on moderate-size datasets typically available in medical imaging applications [35]. Common strategies to facilitate use of transformers in imaging tasks include efficient attention operators that compress contextual

representations at the expense of limiting contextual sensitivity [28], [36], and tokenization via large patches (e.g., a  $16 \times 16$  image patch taken as a single token) that compromises spatial precision [33], [34]. As such, transformer-based methods typically face an undesirable trade-off between long-range sensitivity and local precision. An emerging alternative to efficiently capture contextual representations is state-space models (SSM) [37], [38]. SSMs employ scan trajectories across image pixels to form an input sequence, and use state-space operators for efficient sequence modeling with a refined trade-off between long- and short-range contextual sensitivity [39]. Recent reports have successfully adopted a selective SSM variant (Mamba) for downstream analysis and reconstruction tasks [39]–[44]. Yet, to our knowledge, the potential of SSMs for modality imputation in multi-modal imaging protocols has not been explored prior to the current study.

Here, we introduce a novel learning-based model for multi-modal medical image synthesis, I2I-Mamba, based on selective SSM. Across a high-resolution bottleneck between encoder-decoder modules, I2I-Mamba episodically fuses bidirectional, channel-mixed Mamba (cmMamba) blocks with residual CNN blocks at select stages (Fig. 1). The proposed cmMamba blocks comprise SSM layers to learn context across the spatial dimension of feature maps, and channel-mixing layers to aggregate context across the channel dimension. Conventional SSMs based on raster-scan trajectories (e.g., sweep, zig-zag) yield state-space operators with anisotropic footprint biased towards rectangular image axes, hence compromising sensitivity to contextual interactions across other directions [45], [46]. In contrast, I2I-Mamba leverages a novel spiral-scan trajectory that devises state-space operators with a near-isotropic footprint, thereby achieving more uniform contextual sensitivity (Fig. 2). These architectural elements enable I2I-Mamba to achieve a more favorable balance between short- and long-range contextual sensitivity. Comprehensive demonstrations are reported for imputing missing modalities in multi-contrast MRI and MRI-CT protocols. Our results indicate that I2I-Mamba offers superior performance against state-of-the-art convolutional, transformer, and SSM models. Code to implement I2I-Mamba is publicly available at <https://github.com/icon-lab/I2I-Mamba>.

### Contributions

- To our knowledge, we introduce the first SSM-based model that translates between multi-modal data to synthesize medical images from missing modalities.
- We introduce a novel network architecture that episodically injects channel-mixed Mamba blocks in its bottleneck to simultaneously learn context across spatial and channel dimensions of feature maps.
- We introduce a novel spiral-scan trajectory for SSM layers that enhances isotropy of state-space operators and thereby improves capture of contextual features.

## II. RELATED WORK

### A. Learning-based medical image synthesis

Learning-based synthesis relies on the employed model architectures to infer context from medical images. A main-

stream architecture has been CNNs that use convolution operators to extract short-range context, albeit CNNs are known to suffer from insensitivity to long-range context and poor generalization to atypical anatomy [30]. Attention mechanisms have been considered in CNN backbones to modulate intermediate feature maps and increase focus on potentially problematic regions in terms of synthesis performance [31], [47]–[49]. However, recent work suggests that such multiplicative gating of feature maps with attention offers limited sensitivity for global context since the underlying feature maps are still derived via convolution operators [35], [50].

Transformers have later been adopted to improve capture of long-range contextual interactions among distant regions [28], [33]. To alleviate the heavy computational burden of pure transformer backbones, a group of methods have adopted relatively efficient variants based on approximations to self-attention, such as locally windowed or low-rank attention operators [28], [36]. These approximations improve efficiency by restricting the scope of examined contextual interactions, so they inevitably cap the contextual sensitivity benefits of transformers [28]. A second group has instead adopted hybrid CNN-transformer architectures, where transformer modules are selectively used in model stages with low-spatial-resolution feature maps [33], [35], compromising local precision in contextual representations. Thus, previous transformer-based methods remain susceptible to an undesirable trade-off between long-range sensitivity and local precision, due to the intrinsic complexity of attention operators.

### B. SSM models in medical imaging

SSM is an emerging paradigm that promises to maintain a refined balance between short- and long-range sensitivity without suffering from heavy model complexity. In medical imaging, SSM models have recently been proposed for downstream analysis tasks (e.g., segmentation [40]–[42], [51], classification [44]) and upstream within-modality tasks (e.g., reconstruction from subsampled measurements [43], random image generation [52]). Differing from these studies, here we propose I2I-Mamba for the unique task of translating between source and target modalities. We further introduce several novel design elements in I2I-Mamba absent from previous SSM models. Note that recent SSM models in medical imaging typically follow a UNet-design that dramatically lowers spatial resolution of encoded feature maps (e.g.  $16 \times 16$ ) [39], which can limit spatial precision in contextual representations [18]. These models also employ conventional SSM layers with raster-scan trajectories to cast images onto sequences [38]. Raster-scan trajectories elicit state-space operators with anisotropic footprints along horizontal/vertical image axes, and this rectangular bias can compromise learning of contextual features in other orientations [45], [46]. In contrast, I2I-Mamba leverages a deep bottleneck equipped with cmMamba blocks to contextualize latent representations at higher resolution (i.e.,  $64 \times 64$ ), thereby maintaining higher local precision. Furthermore, it leverages a novel spiral-scan trajectory that yields state-space operators with near-isotropic footprint, thereby

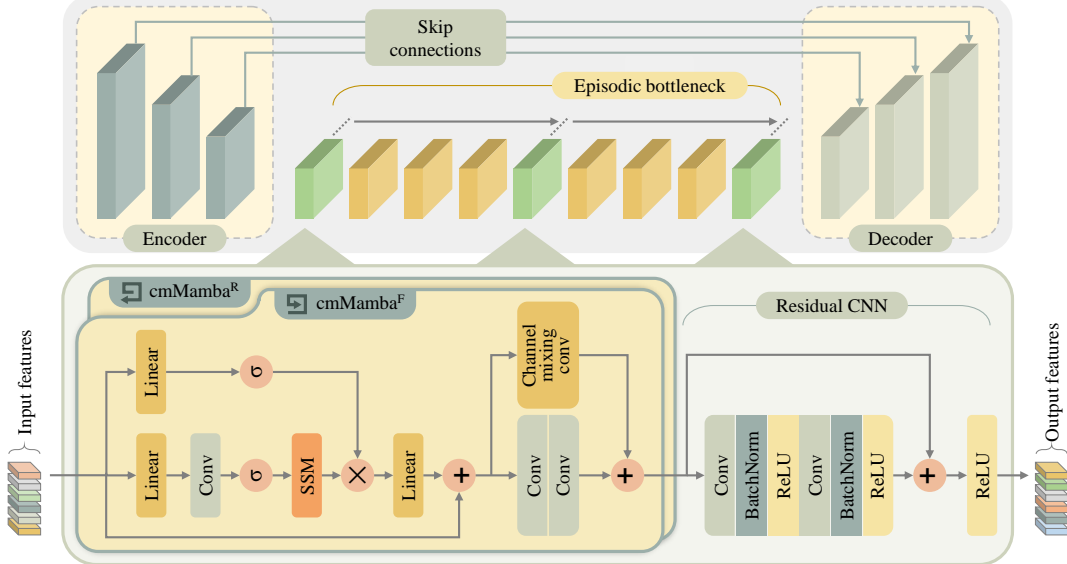


**Fig. 1:** Network architecture for I2I-Mamba. The proposed model comprises encoder, episodic bottleneck, and decoder modules to synthesize target from source images. The encoder extracts high-level latent representations of the source image via convolutional layers. The episodic bottleneck extracts task-relevant contextual information: long-range spatial context and channel context via intermittently injected bidirectional cmMamba blocks (cmMamba<sup>F</sup>: forward direction, cmMamba<sup>R</sup>: reverse direction), and short-range spatial context via residual CNN blocks available at all stages. The decoder back-projects the contextualized representations onto the target image via convolutional layers.

enabling improved capture of contextual features across non-rectangular orientations. With these advances, we provide the first demonstrations of SSM-based multi-contrast MRI and MRI-CT translation in the literature.

### III. METHODS

#### A. I2I-Mamba

I2I-Mamba is a novel adversarial model that combines the contextual sensitivity of SSMs with the local precision of CNNs for improved performance in multi-modal medical image synthesis. Details of the proposed architecture and learning procedures are described below.

**1) Model Architecture:** Given the prowess of adversarial methods in image synthesis [18], I2I-Mamba is devised as an adversarial model with generator/discriminator subnetworks. The generator comprises encoder, episodic bottleneck, and decoder modules to synthesize target-modality images from source-modality images (Fig. 1).

**Encoder.** Receiving as input available source-modality images, the encoder extracts high-level latent representations after concatenating input modalities into a tensor:

$$X = [x_1; x_2; \dots; x_I], \quad (1)$$

where  $I \in \mathbb{Z}^+$  is the number of source modalities,  $x_i \in \mathbb{R}^{H,W}$  is the source image for the  $i$ th modality, and  $X \in \mathbb{R}^{H,W,I}$  is the input tensor ( $H, W$ : image height and width). The input tensor is projected through multiple CNN blocks to derive latent representations at relatively high spatial resolution:

$$f_1 = \text{CNN}(X), \quad (2)$$

where  $f_1 \in \mathbb{R}^{H' = H/\alpha, W' = W/\alpha, C}$  ( $\alpha$ : moderate downsampling rate,  $C$ : the number of feature channels).

**Bottleneck.** Next, a deep bottleneck with  $J$  stages extracts task-relevant contextual representations. A residual CNN (rCNN) block is included at each stage to capture short-range

spatial context [53]. Meanwhile, *novel cmMamba blocks* are employed that contain SSM layers to achieve sensitivity to long-range spatial context [38], and channel-mixing layers to aggregate contextual interactions among feature-map channels [54]. Here we observe that an episodic bottleneck with cmMamba injected at stages  $S = \{1, \lceil J/2 \rceil, J\}$  performs favorably ( $\lceil \cdot \rceil$  denoting the ceiling operation). Receiving  $f_j \in \mathbb{R}^{H', W', C}$ , the  $j$ th stage computes  $f_{j+1} \in \mathbb{R}^{H', W', C}$  as:

$$f_{j+1} = \begin{cases} \text{rCNN}(\text{cmMamba}^F(f_j) + \text{cmMamba}^R(f_j)), & j \in S \\ \text{rCNN}(f_j), & \text{o/w} \end{cases} \quad (3)$$

where cmMamba<sup>F,R</sup> denote blocks operating in forward and reverse directions of the SSM scan trajectory.

**Decoder.** The decoder receives contextualized feature maps  $f_J$  from the bottleneck and projects them onto synthetic target image  $y \in \mathbb{R}^{H,W}$  via transposed convolution blocks:

$$y = \text{CNN}_{\text{transposed}}(f_J). \quad (4)$$

**cmMamba blocks.** In each cmMamba block, a first branch computes a gating variable  $g \in \mathbb{R}^{H', W', \beta C}$ :

$$g = \sigma(\text{Lin}_\beta(f_j)), \quad (5)$$

where  $\sigma$  is an activation function, Lin is a linear projection with expansion factor  $\beta$ . A second branch embeds  $f_j$  via depth-wise convolution, and passes it through an SSM layer:

$$e_j = \sigma(\text{DWConv}(\text{Lin}_\beta(f_j))), \quad (6)$$

$$M = \text{SSM}(e_j). \quad (7)$$

In conventional SSM layers, the input feature map is expanded along spatial dimensions onto a 1D sequence with a raster-scan trajectory (e.g., based on rectilinear sweep or zig-zag patterns) [38]. This causes state-space operators to have anisotropic footprints biased towards rectangular image axes, which can compromise learning of contextual features

in remaining orientations (Fig. 2c; [39]). To alleviate orientation bias in state-space operators, here we propose a *novel spiral-scan trajectory* that maps  $e_j \in \mathbb{R}^{H',W',\beta C}$  onto a sequence  $z_{in}$  as (Fig. 2d):

$$z_{in}[n, c] = e_j(h[n], w[n], c), \quad \text{such that:} \quad (8)$$

$$h^F[n] = (1 - \Gamma) \lfloor \frac{H' + 2}{2} \rfloor + \sum_{k=1}^{(H'W' - n + 1)} \Gamma \cos(\frac{\pi}{2} \lfloor \sqrt{4k - 7} \rfloor),$$

$$w^F[n] = (1 - \Gamma) \lfloor \frac{W' + 2}{2} \rfloor - \sum_{k=1}^{(H'W' - n + 1)} \Gamma \sin(\frac{\pi}{2} \lfloor \sqrt{4k - 7} \rfloor).$$

where  $n \in \mathbb{Z}^{[1 \ H'W']}$  is the sequence index,  $\Gamma = \text{sgn}(k-1)$  with  $\text{sgn}$  denoting signum function,  $\lfloor \cdot \rfloor$  is the floor operation, and ( $h^F \in \mathbb{Z}^{[1 \ H']}$ ,  $w^F \in \mathbb{Z}^{[1 \ W']}$ ) denote the ordering of rectangular pixel coordinates in the forward direction. The ordering for the reverse direction can be obtained as:  $h^R[n] = h^F[H'W' - n + 1]$ ,  $w^R[n] = w^F[H'W' - n + 1]$ .

The sequence is then processed via the resultant discretized state-space operator separately across channels [38]:

$$\ell[n, c] = \bar{\mathbf{A}}\ell[n - 1, c] + \bar{\mathbf{B}}[n]z_{in}[n, c], \quad (9)$$

$$z_{out}[n, c] = \bar{\mathbf{C}}[n]\ell[n, c], \quad (10)$$

where  $\ell$  is the hidden state,  $\bar{\mathbf{A}} \in \mathbb{R}^{N, N}$  is a learnable and  $\bar{\mathbf{B}}[n] \in \mathbb{R}^{N, 1}$ ,  $\bar{\mathbf{C}}[n] \in \mathbb{R}^{1, N}$  are learnable, input-dependent parameters,  $N$  is the state dimensionality. By inverting the coordinate mapping in Eq. 8, the output sequence  $z_{out}$  is remapped onto feature map  $M \in \mathbb{R}^{H',W',\beta C}$ .

After gating  $M$  via a Hadamard product, it is linearly projected and residually combined with the input feature map:

$$e_{SSM} = f_j + \text{Lin}_{1/\beta}(g \odot M). \quad (11)$$

Note that  $e_{SSM} \in \mathbb{R}^{H',W',C}$  primarily captures spatial relationships in feature maps, while treating channels independently. Thus, we propose to include a channel-mixing layer in cmMamba blocks to aggregate context among channels:

$$e_{cm} = \text{cmConv}(e_{SSM}) + \text{Conv}(e_{SSM}), \quad (12)$$

where channel mixing is achieved via a  $1 \times 1$  convolution operator [54]. Next,  $e_{cm} \in \mathbb{R}^{H',W',C}$  is projected through an rCNN block to compute the output feature map  $f_{j+1}$ . Note that residual connections are used around SSM and CNN layers to improve preservation of a diverse array of features.

**2) Learning Procedures:** I2I-Mamba is implemented as an adversarial model with a conditional patch-based discriminator  $D$  [21].  $D$  distinguishes between actual ( $y_{act}$ ) and synthetic ( $y_{syn}$ ) target images. A combined pixel-wise and adversarial objective is used to train the generator  $G$  [33]:

$$L_G = \lambda_{pix} \mathbb{E}[||y_{syn} - y_{act}||_1] - \lambda_{adv} \{ \mathbb{E}[D(y_{act}|X)^2] + \mathbb{E}[(D(y_{syn}|X) - 1)^2] \}, \quad (13)$$

where  $\mathbb{E}$  denotes expectation,  $y_{syn} = G(X)$ ,  $\lambda_{pix}$  and  $\lambda_{adv}$  are loss-term weightings. Meanwhile, an adversarial term is used to train the discriminator  $D$  [21]:

$$L_D = \mathbb{E}[D(y_{act}|X)^2] + \mathbb{E}[(D(y_{syn}|X) - 1)^2]. \quad (14)$$

## B. Datasets

Experiments were conducted on multi-contrast brain MRI datasets (IXI: <https://brain-development.org/ixi-dataset/>,

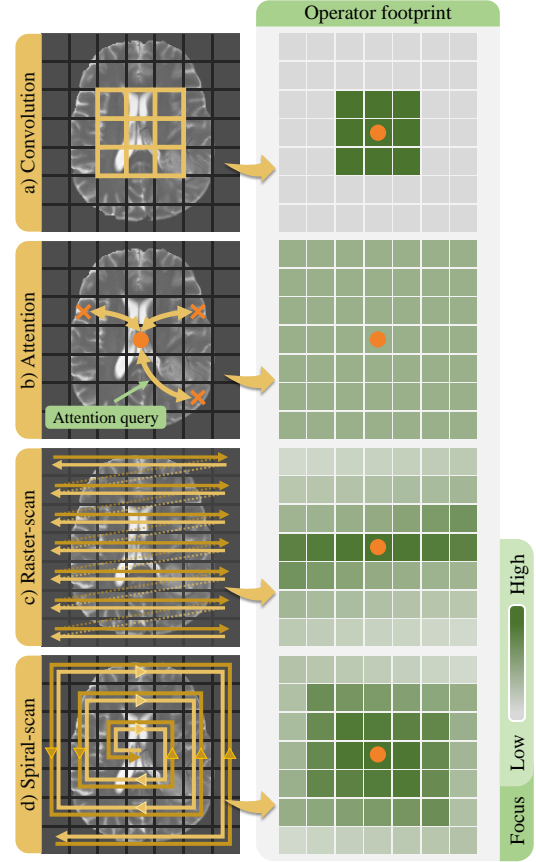


**Fig. 2:** Footprints illustrating the spatial distribution of focus that each learning operator deploys (see colorbar), while seeking contextual interactions of a central pixel (orange dots). **(a)** Convolution operators in CNNs have localized footprints with heavy focus over a restricted neighborhood, compromising sensitivity to long-range contextual interactions. **(b)** Attention operators in transformers have non-local footprints that diffusely distribute focus over the image, compromising local precision. **(c)** Conventional state-space operators in SSMs are based on raster-scan trajectories with anisotropic footprints biased towards rectangular image axes, limiting sensitivity to interactions in non-rectangular orientations. **(d)** I2I-Mamba’s state-space operator leverages a novel spiral-scan trajectory that attains a near-isotropic footprint with more uniform focus across orientations. It also maintains an improved balance between long- and short-range contextual interactions compared to attention operators.

BraTS [55]) and a multi-modal pelvic MRI-CT dataset [56].

**IXI.**  $T_{1-}$ ,  $T_{2-}$ , PD-weighted MR images from 53 subjects were analyzed, with a (25, 10, 18) subject split for (training, validation, test) sets. In each subject, 100 cross-sections with brain tissue were included. Prior to modeling,  $T_2$ - and PD-weighted images were spatially registered onto  $T_1$ -weighted images via an affine transformation in FSL.

**BraTS.**  $T_{1-}$ ,  $T_{2-}$ , FLAIR-weighted MR images from 55 subjects were analyzed, with a (25, 10, 25) subject split. In each subject, 100 cross-sections with brain tissue were included. As publicly shared, this dataset provides images that are co-registered onto  $T_1$ -weighted MRI scans.

**MRI-CT.**  $T_{1-}$ ,  $T_{2-}$ -weighted MRI, and CT images from 15 subjects were analyzed, with a (9, 2, 4) subject split. In each subject, 90 cross-sections were included. As publicly shared, this dataset provides multi-modal images that are co-registered onto  $T_2$ -weighted MRI scans.

**TABLE I:** Performance for multi-contrast MRI synthesis tasks in IXI. PSNR (dB) and SSIM are listed as mean $\pm$ std across the test set. Boldface indicates the top-performing model for each task.

|           | T <sub>1</sub> , T <sub>2</sub> $\rightarrow$ PD |                             | T <sub>1</sub> , PD $\rightarrow$ T <sub>2</sub> |                             | T <sub>2</sub> , PD $\rightarrow$ T <sub>1</sub> |                             | T <sub>2</sub> $\rightarrow$ PD |                             | PD $\rightarrow$ T <sub>2</sub> |                             |
|-----------|--|-----------------------------|--|-----------------------------|--|-----------------------------|---------------------------------|-----------------------------|---------------------------------|-----------------------------|
|           | PSNR   | SSIM                        | PSNR   | SSIM                        | PSNR   | SSIM                        | PSNR                            | SSIM                        | PSNR                            | SSIM                        |
| I2I-Mamba | <b>33.48</b><br>$\pm 2.46$                       | <b>0.970</b><br>$\pm 0.010$ | <b>34.55</b><br>$\pm 1.85$                       | <b>0.969</b><br>$\pm 0.010$ | <b>29.08</b><br>$\pm 2.44$                       | <b>0.946</b><br>$\pm 0.027$ | <b>32.64</b><br>$\pm 2.45$      | <b>0.965</b><br>$\pm 0.013$ | <b>34.01</b><br>$\pm 1.66$      | <b>0.967</b><br>$\pm 0.010$ |
| pGAN      | 31.91<br>$\pm 2.51$                              | 0.948<br>$\pm 0.025$        | 33.95<br>$\pm 1.80$                              | 0.966<br>$\pm 0.010$        | 28.12<br>$\pm 2.42$                              | 0.930<br>$\pm 0.035$        | 30.46<br>$\pm 2.57$             | 0.924<br>$\pm 0.013$        | 33.05<br>$\pm 1.64$             | 0.963<br>$\pm 0.011$        |
| medSynth  | 30.69<br>$\pm 2.43$                              | 0.940<br>$\pm 0.019$        | 32.66<br>$\pm 2.40$                              | 0.963<br>$\pm 0.017$        | 27.10<br>$\pm 2.18$                              | 0.915<br>$\pm 0.037$        | 29.10<br>$\pm 2.44$             | 0.909<br>$\pm 0.013$        | 30.41<br>$\pm 2.08$             | 0.956<br>$\pm 0.016$        |
| SAGAN     | 32.07<br>$\pm 2.58$                              | 0.952<br>$\pm 0.024$        | 33.71<br>$\pm 1.75$                              | 0.965<br>$\pm 0.010$        | 28.22<br>$\pm 2.73$                              | 0.933<br>$\pm 0.027$        | 30.35<br>$\pm 2.05$             | 0.914<br>$\pm 0.033$        | 32.96<br>$\pm 1.65$             | 0.962<br>$\pm 0.011$        |
| ResViT    | 32.98<br>$\pm 2.35$                              | 0.968<br>$\pm 0.027$        | 33.47<br>$\pm 2.54$                              | 0.964<br>$\pm 0.014$        | 28.45<br>$\pm 1.46$                              | 0.936<br>$\pm 0.011$        | 32.08<br>$\pm 2.49$             | 0.952<br>$\pm 0.010$        | 32.84<br>$\pm 1.56$             | 0.964<br>$\pm 0.011$        |
| TransUNet | 30.84<br>$\pm 2.27$                              | 0.953<br>$\pm 0.031$        | 32.36<br>$\pm 1.97$                              | 0.960<br>$\pm 0.015$        | 27.34<br>$\pm 1.95$                              | 0.928<br>$\pm 0.033$        | 29.01<br>$\pm 2.37$             | 0.927<br>$\pm 0.019$        | 31.73<br>$\pm 1.87$             | 0.958<br>$\pm 0.015$        |
| PTNet     | 30.33<br>$\pm 2.59$                              | 0.935<br>$\pm 0.018$        | 32.62<br>$\pm 2.09$                              | 0.954<br>$\pm 0.013$        | 27.73<br>$\pm 2.79$                              | 0.931<br>$\pm 0.029$        | 29.75<br>$\pm 2.66$             | 0.932<br>$\pm 0.012$        | 32.46<br>$\pm 2.19$             | 0.956<br>$\pm 0.022$        |
| U-Mamba   | 31.96<br>$\pm 2.43$                              | 0.960<br>$\pm 0.012$        | 28.53<br>$\pm 2.27$                              | 0.937<br>$\pm 0.030$        | 27.73<br>$\pm 2.52$                              | 0.929<br>$\pm 0.040$        | 32.26<br>$\pm 2.30$             | 0.963<br>$\pm 0.014$        | 26.48<br>$\pm 5.87$             | 0.900<br>$\pm 0.098$        |

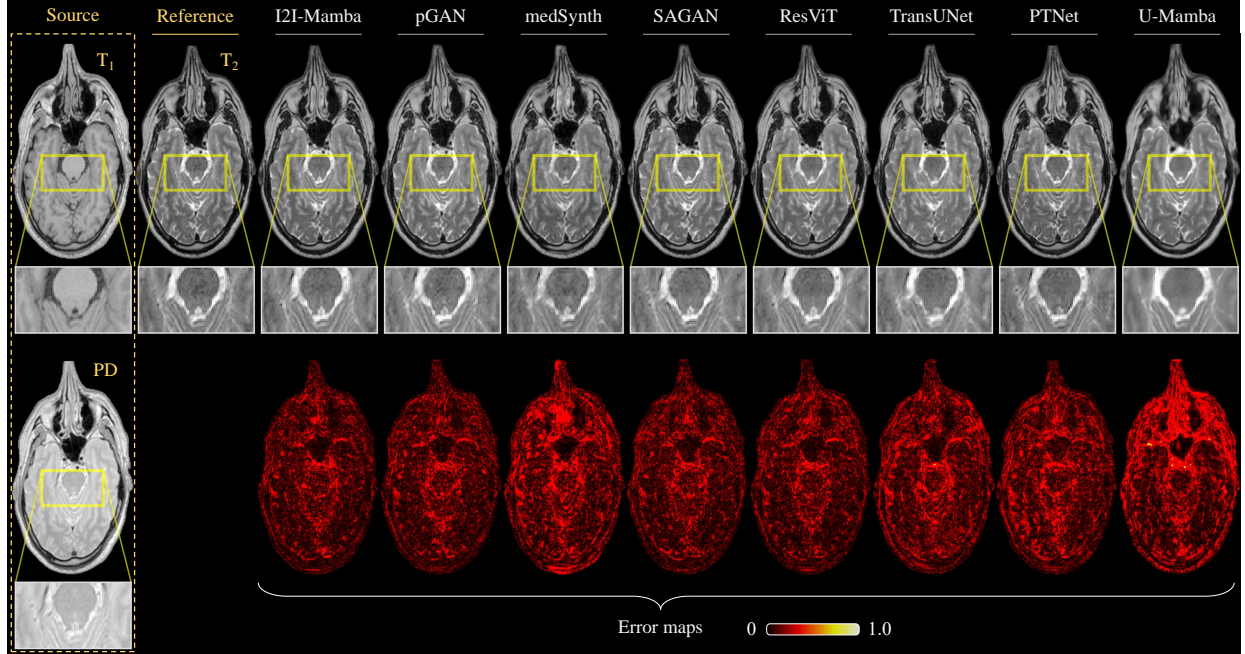


**Fig. 3:** Representative results for T<sub>1</sub>, PD  $\rightarrow$  T<sub>2</sub> in IXI. Synthetic target images from competing methods are displayed along with source images and reference target images. Zoom-in windows and error maps are also included to highlight differences among methods.

### C. Architectural Design

The encoder module in I2I-Mamba had 3 stages, each containing a CNN block with a convolutional layer, batch normalization, and ReLU activation.  $H=256$ ,  $W=256$ ,  $\alpha=4$ ,  $C=256$  were used. The bottleneck had 9 stages, each containing a residual CNN block with 2 cascades of a convolutional layer, batch normalization, and ReLU activation. Bidirectional cmMamba blocks were inserted in stages  $j=\{1,5,9\}$ , and used  $\beta=2$ ,  $N=16$ , and SiLU activations. Channel-mixing blocks used a parallel combination of a channel-mixing convolutional layer and 2 regular convolutional layers. The decoder module

had 3 stages, each containing a CNN block with a convolutional layer, batch normalization, and ReLU activation, except for the final stage that used a Tanh activation. Long-range skip connections were employed between corresponding encoder-decoder stages to better preserve low-level spatial information.

### D. Competing Methods

Several state-of-the-art baselines for medical image synthesis were considered including convolutional models (pGAN [18], medSynth [21], SAGAN [31]) and transformer models (ResViT [33], TransUNet [35], PTNet [28]), along with a

TABLE II: Performance for multi-contrast MRI synthesis tasks in BraTS.

|           | T <sub>1</sub> , T <sub>2</sub> → FLAIR |                        | T <sub>1</sub> , FLAIR → T <sub>2</sub> |                        | T <sub>2</sub> , FLAIR → T <sub>1</sub> |                        | T <sub>2</sub> → FLAIR |                        | FLAIR → T <sub>2</sub> |                        |
|-----------|---|------------------------|---|------------------------|---|------------------------|------------------------|------------------------|------------------------|------------------------|
|           | PSNR                                    | SSIM                   | PSNR                                    | SSIM                   | PSNR                                    | SSIM                   | PSNR                   | SSIM                   | PSNR                   | SSIM                   |
| I2I-Mamba | <b>26.39</b><br>±2.47                   | 0.910<br>±0.033        | <b>26.31</b><br>±2.08                   | <b>0.910</b><br>±0.029 | <b>23.73</b><br>±3.76                   | 0.900<br>±0.036        | <b>25.74</b><br>±2.48  | <b>0.903</b><br>±0.034 | <b>25.97</b><br>±1.90  | <b>0.908</b><br>±0.028 |
| pGAN      | 25.76<br>±2.42                          | 0.905<br>±0.032        | 25.55<br>±1.88                          | 0.907<br>±0.027        | 23.00<br>±3.29                          | 0.896<br>±0.030        | 24.72<br>±2.34         | 0.894<br>±0.034        | 25.15<br>±1.84         | 0.900<br>±0.029        |
| medSynth  | 25.69<br>±2.25                          | <b>0.912</b><br>±0.031 | 25.16<br>±1.79                          | 0.894<br>±0.030        | 23.46<br>±3.17                          | 0.902<br>±0.032        | 25.07<br>±2.26         | 0.889<br>±0.034        | 24.77<br>±1.70         | 0.890<br>±0.030        |
| SAGAN     | 25.87<br>±0.63                          | 0.907<br>±0.003        | 25.06<br>±0.68                          | 0.902<br>±0.003        | 23.20<br>±1.17                          | 0.894<br>±0.010        | 25.13<br>±0.41         | 0.890<br>±0.003        | 24.93<br>±0.42         | 0.894<br>±0.003        |
| ResViT    | 25.79<br>±2.16                          | 0.900<br>±0.031        | 25.29<br>±1.74                          | 0.904<br>±0.027        | 23.06<br>±3.48                          | 0.899<br>±0.032        | 24.95<br>±2.11         | 0.883<br>±0.034        | 24.89<br>±1.72         | 0.888<br>±0.028        |
| TransUNet | 25.54<br>±2.24                          | 0.899<br>±0.032        | 25.59<br>±1.86                          | 0.909<br>±0.024        | 23.26<br>±3.52                          | <b>0.907</b><br>±0.033 | 25.28<br>±2.26         | 0.896<br>±0.032        | 25.04<br>±1.84         | 0.899<br>±0.029        |
| PTNet     | 25.03<br>±2.31                          | 0.888<br>±0.038        | 24.52<br>±1.70                          | 0.886<br>±0.032        | 20.94<br>±3.66                          | 0.871<br>±0.044        | 24.45<br>±2.08         | 0.882<br>±0.037        | 23.89<br>±1.63         | 0.876<br>±0.033        |
| U-Mamba   | 25.37<br>±2.39                          | 0.891<br>±0.037        | 25.58<br>±1.70                          | 0.909<br>±0.026        | 23.36<br>±3.59                          | 0.895<br>±0.035        | 24.86<br>±1.55         | 0.882<br>±0.022        | 25.03<br>±1.33         | 0.894<br>±0.024        |

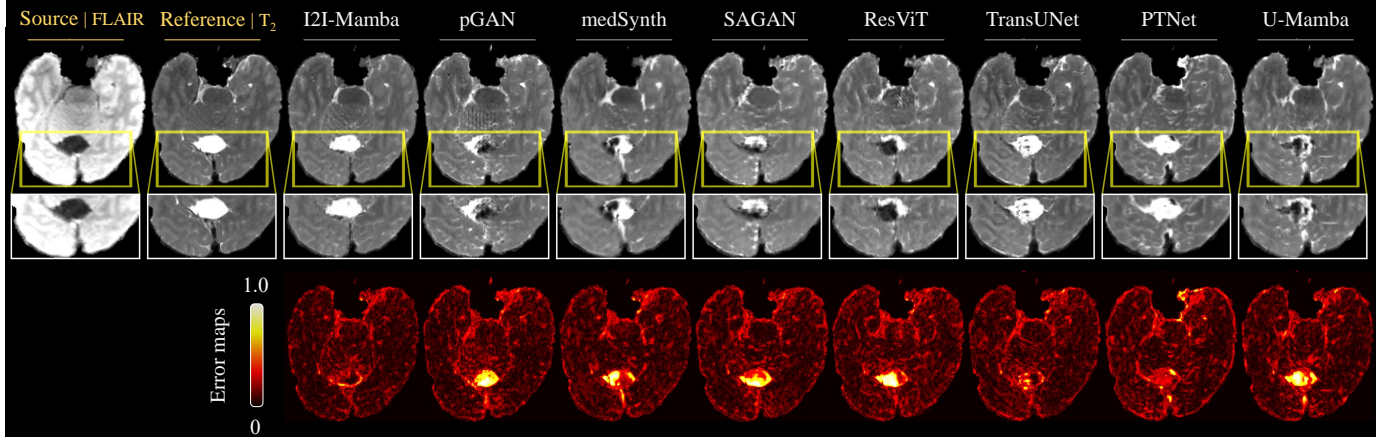


Fig. 4: Representative results for FLAIR → T<sub>2</sub> in BraTS. Synthetic target images from competing methods are displayed along with source images and reference target images. Zoom-in windows and error maps are also included to highlight differences among methods.

recent SSM model introduced for medical image segmentation (U-Mamba [40]). For fair comparison, all competing methods were implemented as adversarial models with a PatchGAN discriminator and the losses in Eqs. 13-14.

### E. Modeling Procedures

Modeling was performed using the PyTorch framework on an Nvidia RTX 4090 GPU. All models were trained from scratch via the Adam optimizer with parameters  $\beta_1 = 0.5$ ,  $\beta_2 = 0.999$ . Model hyperparameters were selected via cross-validation. To avoid potential biases, a common set of hyperparameters observed to yield near-optimal validation performance across models was selected. Accordingly,  $2 \times 10^{-4}$  learning rate, 60 epochs,  $\lambda_{adv} = 1$ ,  $\lambda_{pix} = 100$  were prescribed. To evaluate performance, peak signal-to-noise ratio (PSNR) and structural similarity index (SSIM) metrics were measured between ground-truth and synthetic images. Significance of performance differences was assessed with non-parametric signed-rank tests ( $p < 0.05$ ).

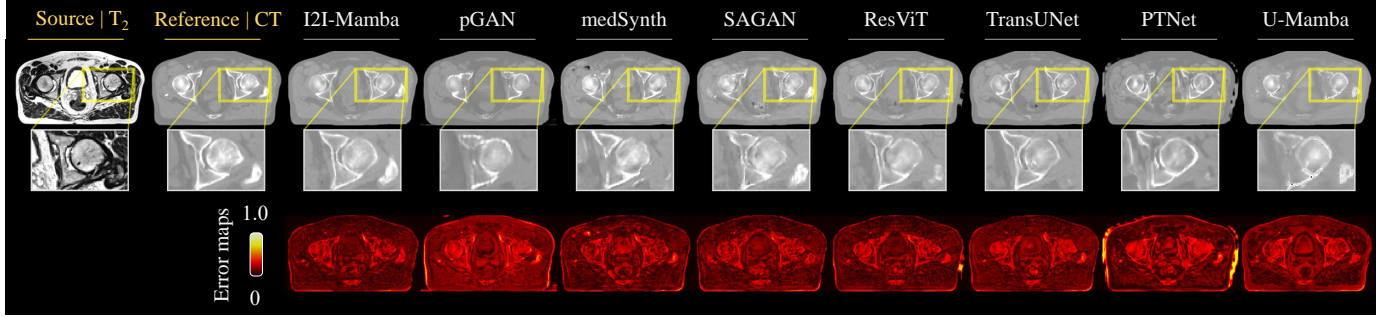
## IV. RESULTS

### A. Multi-Contrast MRI Synthesis

We first conducted experiments for target-modality imputation in multi-contrast MRI. I2I-Mamba was comparatively demonstrated against convolutional (pGAN, medSynth, SAGAN), transformer (ResViT, TransUNet, PTNet), and SSM (U-Mamba) models. Table I lists performance metrics for synthesis tasks in IXI that comprises data from healthy subjects. I2I-Mamba achieves the highest performance metrics consistently across tasks ( $p < 0.05$ ). On average, I2I-Mamba offers performance improvements of 2.0dB PSNR, 2.0% SSIM over competing methods. Meanwhile, Table II lists performance metrics for synthesis tasks in BraTS that comprises data from glioma subjects. I2I-Mamba achieves the highest performance metrics in all tasks ( $p < 0.05$ ), except for T<sub>1</sub>, T<sub>2</sub> → FLAIR where medSynth yields moderately higher SSIM and T<sub>2</sub>, FLAIR → T<sub>1</sub> where TransUNet yields higher SSIM. On average, I2I-Mamba offers performance improvements of 1.0dB PSNR, 1.2% SSIM over competing methods.

**TABLE III:** Performance for the  $T_2$ -MRI  $\rightarrow$  CT and  $T_1$ -MRI  $\rightarrow$  CT synthesis tasks in the MRI-CT dataset.

|                      | I2I-Mamba                   | pGAN                 | medSynth             | SAGAN                | ResViT               | TransUNet            | PTNet                | U-Mamba              |
|----------------------|-----------------------------|----------------------|----------------------|----------------------|----------------------|----------------------|----------------------|----------------------|
| $T_2 \rightarrow CT$ | <b>28.51</b><br>$\pm 1.94$  | 27.22<br>$\pm 2.73$  | 26.87<br>$\pm 1.79$  | 28.03<br>$\pm 1.97$  | 27.87<br>$\pm 2.06$  | 28.06<br>$\pm 2.20$  | 27.35<br>$\pm 2.23$  | 26.32<br>$\pm 1.77$  |
|                      | <b>0.916</b><br>$\pm 0.023$ | 0.906<br>$\pm 0.026$ | 0.886<br>$\pm 0.026$ | 0.911<br>$\pm 0.020$ | 0.913<br>$\pm 0.027$ | 0.915<br>$\pm 0.021$ | 0.911<br>$\pm 0.026$ | 0.902<br>$\pm 0.022$ |
| $T_1 \rightarrow CT$ | <b>28.04</b><br>$\pm 2.25$  | 26.16<br>$\pm 2.20$  | 27.26<br>$\pm 2.54$  | 26.30<br>$\pm 2.29$  | 26.75<br>$\pm 1.63$  | 26.55<br>$\pm 2.01$  | 25.61<br>$\pm 1.98$  | 26.38<br>$\pm 1.85$  |
|                      | <b>0.911</b><br>$\pm 0.027$ | 0.870<br>$\pm 0.043$ | 0.891<br>$\pm 0.030$ | 0.888<br>$\pm 0.028$ | 0.888<br>$\pm 0.021$ | 0.900<br>$\pm 0.025$ | 0.863<br>$\pm 0.030$ | 0.894<br>$\pm 0.026$ |

**Fig. 5:** Representative results for  $T_2 \rightarrow CT$  in the MRI-CT dataset. Synthetic target images from competing methods are displayed along with source images and reference target images. Zoom-in windows and error maps are also included to highlight differences among methods.

Synthetic target images from representative tasks are displayed in Fig. 3 for the IXI dataset, and in Fig. 4 for the BraTS dataset. Among competing methods, convolutional baselines suffer from striping or grid-like pixel artifacts (e.g., pGAN, SAGAN); and transformer and SSM baselines suffer from a degree of spatial blur and inaccuracies in depiction of detailed anatomical structures (e.g., ResViT, PTNet, U-Mamba). Particularly evident in BraTS images containing pathology, all examined baselines suffer from notable hallucinatory features manifesting as hypo-intense or hyper-intense signals grossly deviating from ground truth. In comparison to baselines, I2I-Mamba synthesizes target images with more accurate depiction of detailed structure and contrast in tissues, along with lower artifacts. Note that U-Mamba is a pure SSM model based on a UNet-style architecture that substantially lowers spatial resolution of encoded feature maps, and it uses conventional SSM layers that are devoid of channel-mixing and spiral-scan trajectories. Instead, I2I-Mamba is a hybrid SSM-CNN model that maintains relatively higher-resolution feature maps, and it uses novel channel-mixed Mamba blocks with spiral-scan trajectories. Thus, the superior performance of I2I-Mamba over U-Mamba can be attributed to the fundamental architectural differences between the two methods. Taken together, these results indicate that I2I-Mamba offers enhanced capture of contextual features that serve a critical role in synthesizing high-quality target images in multi-contrast MRI protocols.

### B. MRI-CT Synthesis

Next, we conducted experiments for target-modality imputation on the multi-modal MRI-CT dataset. Performance metrics for MRI  $\rightarrow$  CT synthesis tasks are listed in Table III. Among competing methods, I2I-Mamba achieves the highest

**TABLE IV:** Average inference times (Inf. in msec) and memory load (Mem. in gigabytes) per cross-section for competing methods.

|      | I2I-Mamba | pGAN | medSynth | SAGAN | ResViT | TransUNet | PTNet | U-Mamba |
|------|-----------|------|----------|-------|--------|-----------|-------|---------|
| Inf. | 11        | 9    | 12       | 9     | 15     | 12        | 34    | 10      |
| Mem. | 2.5       | 2.3  | 2.9      | 2.7   | 4.6    | 4.0       | 10.8  | 1.6     |

performance metrics consistently across tasks ( $p < 0.05$ ). On average, I2I-Mamba attains improvements of 1.4dB PSNR, 1.6% SSIM over competing methods. Note that, corroborating the findings in multi-contrast MRI synthesis tasks, we observe that U-Mamba yields relatively limited synthesis performance among baselines. Taken together, these findings suggest that conventional SSM architectures based solely on state-space operators may offer suboptimal sensitivity to contextual features, which might in turn degrade reliability in multi-modal medical image synthesis.

Representative synthetic images are displayed in Fig. 5. Among competing methods, convolutional baselines suffer from residual striping and ringing artifacts evident near regions of high tissue signal (e.g., pGAN, SAGAN). Although transformer and SSM baselines are relatively more reliable against these artifacts, they are susceptible to hallucinatory hypo- or hyper-intense signal regions especially across diagnostically-critical bone tissue (e.g., ResViT, TransUNet, U-Mamba), and U-Mamba in particular shows a degree of spatial blur that partly obscures visualization of detailed structures. In comparison, I2I-Mamba synthesizes target images with lower artifacts and more accurate delineation of tissue structure and contrast, particularly across diagnostically relevant bone regions. Taken together, these results indicate that I2I-Mamba maintains a more favorable balance between sensitivity to short- versus long-range context than baselines, thereby enabling more reliable imputation of missing medical image modalities.

**TABLE V:** Performance of I2I-Mamba variants built by: ablating cmMamba blocks (w/o cmMamba), ablating channel-mixing layers (w/o chan mix), ablating rCNN blocks at  $j = \{1, 5, 9\}$  (w/o rCNN), tying the weights of cmMamba blocks (w tied cmMamba). Results listed for representative synthesis tasks of  $T_1, T_2 \rightarrow PD$  in IXI, FLAIR  $\rightarrow T_2$  in BraTS, and  $T_1 \rightarrow CT$  in the MRI-CT dataset.

|                | $T_1, T_2 \rightarrow PD$  |                             | FLAIR $\rightarrow T_2$    |                             | $T_1 \rightarrow CT$       |                             |
|----------------|----------------------------|-----------------------------|----------------------------|-----------------------------|----------------------------|-----------------------------|
|                | PSNR                       | SSIM                        | PSNR                       | SSIM                        | PSNR                       | SSIM                        |
| I2I-Mamba      | <b>33.48</b><br>$\pm 2.46$ | <b>0.970</b><br>$\pm 0.010$ | <b>25.97</b><br>$\pm 1.90$ | <b>0.908</b><br>$\pm 0.028$ | <b>28.04</b><br>$\pm 2.25$ | <b>0.911</b><br>$\pm 0.027$ |
| w/o cmMamba    | 32.65<br>$\pm 2.56$        | 0.968<br>$\pm 0.010$        | 24.86<br>$\pm 2.05$        | 0.899<br>$\pm 0.029$        | 27.18<br>$\pm 1.98$        | 0.902<br>$\pm 0.021$        |
| w/o chan mix   | 33.19<br>$\pm 2.50$        | <b>0.970</b><br>$\pm 0.011$ | 25.29<br>$\pm 1.84$        | 0.900<br>$\pm 0.030$        | 27.59<br>$\pm 2.38$        | 0.899<br>$\pm 0.029$        |
| w/o rCNN       | 32.72<br>$\pm 2.57$        | 0.967<br>$\pm 0.012$        | 25.08<br>$\pm 1.85$        | 0.896<br>$\pm 0.023$        | 26.58<br>$\pm 2.00$        | 0.884<br>$\pm 0.031$        |
| w tied cmMamba | 33.11<br>$\pm 2.45$        | 0.969<br>$\pm 0.011$        | 25.74<br>$\pm 1.98$        | 0.904<br>$\pm 0.029$        | 27.50<br>$\pm 2.24$        | 0.895<br>$\pm 0.029$        |

### C. Computational Complexity

For all competing methods, inference times and memory load per cross-section are listed in Table IV. As expected, convolutional baselines based on compact convolution operators have relatively low computational burden. Meanwhile, transformer baselines based on attention operators incur heavy computational burden that is reflected in prolonged inference times and memory load, evident for both hybrid CNN-transformer architectures (ResViT, TransUNet) and pure transformer architectures (PTNet). In comparison, I2I-Mamba and U-Mamba based on state-space operators achieve competitive computational load with convolutional baselines, offering fast inference with low memory consumption, while improving sensitivity to long-range context in medical images.

### D. Ablation Studies

We performed a systematic set of ablation studies to assess the contribution of individual design elements and parameters in I2I-Mamba to synthesis performance. First, we examined the importance of utilizing cmMamba blocks, channel-mixing layers, residual CNN blocks, and encoder-decoder skip connections. To do this, I2I-Mamba was compared against several variants: ‘w/o cmMamba’ that ablated cmMamba blocks in the bottleneck, ‘w/o chan mix’ that ablated channel-mixing layers in cmMamba blocks, ‘w/o rCNN’ that ablated residual CNN blocks from the stages where cmMamba blocks are injected, and ‘w tied cmMamba’ that tied the weights of all cmMamba blocks. Table V lists performance metrics for all variants in representative synthesis tasks. We find that I2I-Mamba outperforms all ablated variants ( $p < 0.05$ ), except for  $T_1, T_2 \rightarrow PD$  in IXI where ‘w/o chan mix’ yields similar SSIM. These results indicate that each examined design element in I2I-Mamba contributes significantly to model performance.

Next, we examined the importance of implementing state-space operators based on the proposed spiral-scan trajectory. For this purpose, I2I-Mamba was compared against several variants based on bidirectional raster-scan trajectories [38]: ‘w sweep<sup>a</sup>’ that used sweep scans in row-major order, ‘w sweep<sup>b</sup>’ that used an ensemble of sweep scans in row- and column-major orders, ‘w zigzag<sup>a</sup>’ that used zigzag scans in row-major

**TABLE VI:** Performance of I2I-Mamba variants built by using: sweep scans in row-major order (w sweep<sup>a</sup>), sweep scans in row/column-major orders (w sweep<sup>b</sup>), zigzag scans in row-major order (w zigzag<sup>a</sup>), zigzag scans in row/column-major orders (w zigzag<sup>b</sup>) and ensemble sweep-zigzag scans (w sweep<sup>a</sup>-zigzag<sup>a</sup>).

|   | $T_1, T_2 \rightarrow PD$  |                             | FLAIR $\rightarrow T_2$    |                             | $T_1 \rightarrow CT$       |                             |
|---|----------------------------|-----------------------------|----------------------------|-----------------------------|----------------------------|-----------------------------|
|   | PSNR                       | SSIM                        | PSNR                       | SSIM                        | PSNR                       | SSIM                        |
| I2I-Mamba                                 | <b>33.48</b><br>$\pm 2.46$ | <b>0.970</b><br>$\pm 0.010$ | <b>25.97</b><br>$\pm 1.90$ | <b>0.908</b><br>$\pm 0.028$ | <b>28.04</b><br>$\pm 2.25$ | <b>0.911</b><br>$\pm 0.027$ |
| w sweep <sup>a</sup>                      | 33.15<br>$\pm 2.51$        | <b>0.970</b><br>$\pm 0.010$ | 25.69<br>$\pm 2.03$        | 0.905<br>$\pm 0.028$        | 27.83<br>$\pm 2.43$        | 0.909<br>$\pm 0.027$        |
| w sweep <sup>b</sup>                      | 33.16<br>$\pm 2.49$        | 0.968<br>$\pm 0.011$        | 25.62<br>$\pm 1.99$        | 0.905<br>$\pm 0.027$        | 27.85<br>$\pm 2.22$        | 0.909<br>$\pm 0.029$        |
| w zigzag <sup>a</sup>                     | 31.68<br>$\pm 2.83$        | 0.941<br>$\pm 0.014$        | 25.71<br>$\pm 1.78$        | 0.906<br>$\pm 0.020$        | 27.58<br>$\pm 1.99$        | 0.905<br>$\pm 0.028$        |
| w zigzag <sup>b</sup>                     | 32.47<br>$\pm 2.61$        | 0.956<br>$\pm 0.013$        | 25.67<br>$\pm 1.92$        | 0.905<br>$\pm 0.025$        | 27.64<br>$\pm 2.16$        | 0.905<br>$\pm 0.025$        |
| w sweep <sup>a</sup> -zigzag <sup>a</sup> | 31.35<br>$\pm 2.78$        | 0.943<br>$\pm 0.015$        | 25.69<br>$\pm 2.12$        | 0.906<br>$\pm 0.025$        | 27.31<br>$\pm 2.14$        | 0.905<br>$\pm 0.038$        |

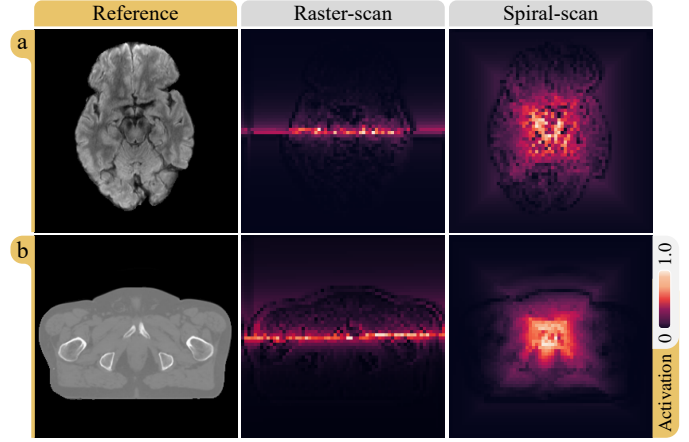


**Fig. 6:** Sample activation maps ( $64 \times 64$ ) for (a) FLAIR  $\rightarrow T_2$  in BraTS, (b)  $T_1 \rightarrow CT$  in MRI-CT. Depicting contextual interactions of a central pixel with remaining pixels across the image, activation maps for the given pixel were extracted from the SSM layer of cmMamba<sup>F</sup> at stage  $j=1$ . Results shown for ‘w sweep<sup>a</sup>’ (raster-scan) and I2I-Mamba (spiral-scan), along with reference target images.

order, ‘w zigzag<sup>b</sup>’ that used an ensemble of zigzag scans in row- and column-major orders, and ‘w sweep<sup>a</sup>-zigzag<sup>a</sup>’ that used an ensemble of sweep and zigzag scans. As listed in Table VI, we find that I2I-Mamba outperforms all variants consistently across tasks ( $p < 0.05$ ), except for  $T_1, T_2 \rightarrow PD$  in IXI where ‘w sweep<sup>a</sup>’ yields similar SSIM. To visually assess the influence of varying operator footprints due to these different scan trajectories, we extracted activation maps in SSM layers of variant models as described in [38]. Fig. 6 displays sample activation maps for a central pixel with I2I-Mamba (i.e., spiral scans) and ‘w sweep<sup>a</sup>’ (i.e., sweep scans). I2I-Mamba has activation maps with relatively isotropic footprint over a broad neighborhood of pixels. In contrast, ‘w sweep<sup>a</sup>’ yields activation maps with a notable bias across the primary scan direction, extending focus to irrelevant background regions and diminishing focus over anatomical regions distanced from the central pixel orthogonally to the scan direction. These results indicate that the near-isotropic footprint of I2I-Mamba’s state-space operator enabled by spiral-scans can offer improved

**TABLE VII:** Performance of I2I-Mamba variants obtained with different sets of stages for cmMamba injection ( $S$ ).  $S^*=\{1,5,9\}$  denotes the set reported in the main experiments.

|                     | T <sub>1</sub> , T <sub>2</sub> → PD |               | FLAIR → T <sub>2</sub> |               | T <sub>1</sub> → CT |               |
|---------------------|--------------------------------------|---------------|------------------------|---------------|---------------------|---------------|
|                     | PSNR                                 | SSIM          | PSNR                   | SSIM          | PSNR                | SSIM          |
| $S=\{1,2,\dots,9\}$ | 32.42                                | 0.965         | 25.81                  | 0.906         | 27.89               | 0.907         |
|                     | ±2.45                                | ±0.012        | ±2.05                  | ±0.029        | ±2.09               | ±0.022        |
| $S=\{1,3,5,7,9\}$   | 33.34                                | 0.970         | 25.81                  | 0.905         | 27.83               | 0.903         |
|                     | ±2.56                                | ±0.011        | ±2.28                  | ±0.029        | ±2.06               | ±0.029        |
| $S^*=\{1,5,9\}$     | <b>33.48</b>                         | 0.970         | <b>25.97</b>           | <b>0.908</b>  | <b>28.04</b>        | <b>0.911</b>  |
|                     | <b>±2.46</b>                         | ±0.010        | <b>±1.90</b>           | <b>±0.028</b> | <b>±2.25</b>        | <b>±0.027</b> |
| $S=\{1,5\}$         | 33.45                                | 0.970         | 25.78                  | 0.905         | 27.81               | 0.907         |
|                     | ±2.51                                | ±0.011        | ±2.03                  | ±0.029        | ±2.07               | ±0.024        |
| $S=\{5,9\}$         | 33.26                                | 0.970         | 25.88                  | 0.906         | 28.00               | 0.908         |
|                     | ±2.55                                | ±0.011        | ±2.01                  | ±0.028        | ±2.04               | ±0.023        |
| $S=\{5\}$           | 33.41                                | <b>0.971</b>  | 25.96                  | <b>0.908</b>  | 28.01               | 0.910         |
|                     | ±2.50                                | <b>±0.011</b> | ±2.11                  | <b>±0.024</b> | ±1.98               | ±0.028        |

capture of contextual features in medical images, compared to raster-scans in conventional SSM models.

Lastly, we examined the importance of episodic injection of cmMamba blocks in select stages of the bottleneck (i.e.,  $S = \{1, 5, 9\}$ ). To do this, we compared I2I-Mamba against variants built by injecting cmMamba blocks in several different configurations across the bottleneck:  $S = \{1, 2, \dots, 9\}$  (all stages),  $S = \{1, 3, 5, 7, 9\}$ ,  $S = \{5, 9\}$ ,  $S = \{1, 5\}$ ,  $S = \{5\}$ . As listed in Table VII, we find that I2I-Mamba yields superior performance against variants with different configurations ( $p < 0.05$ ), except for  $S = \{5\}$  that generally offers similar SSIM. Note that lower performance in variants with fewer cmMamba blocks can be attributed to a relatively limited ability to extract contextual features in medical images, whereas lower performance in variants with a greater number of cmMamba blocks is best attributed to over-fitting due to elevated model complexity. These results suggest that I2I-Mamba attains a favorable trade-off between contextual sensitivity and model complexity via episodic injection of cmMamba blocks.

## V. DISCUSSION & CONCLUSION

Several lines of limitations can be addressed to help further improve the proposed method’s performance. A first group of developments concerns the synthesis tasks implemented. Here we examined one-to-one and many-to-one tasks to impute missing images in multi-contrast MRI and MRI-CT protocols. For optimal performance, a separate model was built for each individual task. In certain scenarios, missing and acquired modalities in a multi-modal protocol may vary sporadically across the imaging cohort [57]. To improve practicality, a unified I2I-Mamba can be built by adopting a masked training strategy so as to perform many-to-many synthesis tasks [33], [57]. When needed, reliability of such multi-tasking models might be boosted via multi-site datasets that would provide access to larger and more diverse sets of training samples [58]. Here, we performed supervised learning by assuming that paired sets of source and target modality images are available in each training subject [18]. In cases where it is difficult to curate paired training images, unsupervised learning strategies based on cycle-consistency could be adopted to permit training on unpaired images [59]–[61]. Corroborating recent findings,

here we observed high performance in translation among endogenous MRI contrasts and in translation from MRI to CT. Literature suggests that synthesizing exogenous MRI contrasts that involve external contrast agents, or synthesis of MRI images from CT are rather ill-posed problems [23], [33]. Incorporating regularization priors regarding the distribution of the target modality might help improve synthesis fidelity in such challenging tasks [5], [20], [60].

A second group of developments concerns the employed loss functions. For fair comparison, here we implemented all competing methods based on a combined pixel-wise/adversarial loss [33]. While we observed that this learning approach elicits high-quality synthetic images, further improvements might be viable with advanced loss terms including gradient-based, difficulty-aware, cross-entropy losses [21], [62], [63]. A potential limitation of adversarial learning is instabilities in model training that can hamper the fidelity of synthetic images [64]. While here we did not observe signs of instability in model training, diffusion learning could be adopted to improve reliability when necessary [49], [52], [65]. Additional improvements to be sought for a diffusion-based implementation include bridge formulations to boost task-relevant information [29], [66]. Lastly, synthesis performance might be further improved by adopting model pre-training procedures [42]. Future studies are warranted for an in-depth evaluation of the ideal training procedures for I2I-Mamba.

In conclusion, we introduced a novel learning-based method for imputing missing modalities in multi-modal imaging protocols. I2I-Mamba episodically cascades novel channel-mixed Mamba blocks with residual CNN blocks to effectively capture both long- and short-range contextual information, and its state-space operators use a novel spiral-scan trajectory to improve sensitivity to contextual interactions across different spatial orientations. With its superior performance over state-of-the-art baselines, I2I-Mamba holds great potential for multi-modal medical image synthesis.

## REFERENCES

- [1] B. J. Pichler, M. S. Judenhofer, and C. Pfannenberg, *Multimodal Imaging Approaches: PET/CT and PET/MRI*. Springer, 2008, pp. 109–132.
- [2] B. Thukral, “Problems and preferences in pediatric imaging,” *Indian J. Radiol. Imaging*, vol. 25, pp. 359–364, 2015.
- [3] J. E. Iglesias, E. Konukoglu, D. Zikic, B. Glocker, K. Van Leemput, and B. Fischl, “Is synthesizing MRI contrast useful for inter-modality analysis?” in *MICCAI*, 2013, pp. 631–638.
- [4] Y. Huo, Z. Xu, S. Bao, A. Assad, R. G. Abramson, and B. A. Landman, “Adversarial synthesis learning enables segmentation without target modality ground truth,” in *ISBI*, 2018, pp. 1217–1220.
- [5] J. Lee, A. Carass, A. Jog, C. Zhao, and J. Prince, “Multi-atlas-based CT synthesis from conventional MRI with patch-based refinement for MRI-based radiotherapy planning,” in *SPIE Med. Imag.*, 2017, p. 101331I.
- [6] Y. Huang, L. Shao, and A. F. Frangi, “Simultaneous super-resolution and cross-modality synthesis of 3D medical images using weakly-supervised joint convolutional sparse coding,” *CVPR*, pp. 5787–5796, 2017.
- [7] A. Adam, A. Dixon, J. Gillard, C. Schaefer-Prokop, R. Grainger, and D. Allison, *Grainger & Allison’s Diagnostic Radiology*. Elsevier, 2014.
- [8] R. Vemulapalli, H. Van Nguyen, and S. K. Zhou, “Unsupervised cross-modal synthesis of subject-specific scans,” in *Int. Conf. Comput. Vis.*, 2015, pp. 630–638.
- [9] Y. Wu, W. Yang, L. Lu, Z. Lu, L. Zhong, M. Huang *et al.*, “Prediction of CT substitutes from MR images based on local diffeomorphic mapping for brain PET attenuation correction,” *J. Nucl. Med.*, vol. 57, no. 10, pp. 1635–1641, 2016.
- [10] D. C. Alexander, D. Zikic, J. Zhang, H. Zhang, and A. Criminisi, “Image quality transfer via random forest regression: Applications in diffusion MRI,” in *MICCAI*, 2014, pp. 225–232.

[11] T. Huynh, Y. Gao, J. Kang, L. Wang, P. Zhang, J. Lian *et al.*, “Estimating CT image from MRI data using structured random forest and auto-context model,” *IEEE Trans. Med. Imag.*, vol. 35, no. 1, pp. 174–183, 2016.

[12] C. Zhao, A. Carass, J. Lee, Y. He, and J. L. Prince, “Whole brain segmentation and labeling from CT using synthetic MR images,” in *MLMI*, 2017, pp. 291–298.

[13] A. Chartsias, T. Joyce, M. V. Giuffrida, and S. A. Tsaftaris, “Multimodal MR synthesis via modality-invariant latent representation,” *IEEE Trans. Med. Imag.*, vol. 37, no. 3, pp. 803–814, 2018.

[14] C. Bowles, C. Qin, C. Ledig, R. Guerrero, R. Gunn, A. Hammers *et al.*, “Pseudo-healthy image synthesis for white matter lesion segmentation,” in *SSMI*, 2016, pp. 87–96.

[15] T. Joyce, A. Chartsias, and S. A. Tsaftaris, “Robust multi-modal MR image synthesis,” in *MICCAI*, 2017, pp. 347–355.

[16] W. Wei, E. Poirion, B. Bodini, S. Durrelman, O. Collot, B. Stankoff *et al.*, “Fluid-attenuated inversion recovery MRI synthesis from multisequence MRI using three-dimensional fully convolutional networks for multiple sclerosis,” *J. Med. Imaging*, vol. 6, no. 1, p. 014005, 2019.

[17] A. Beers, J. Brown, K. Chang, J. Campbell, S. Ostmo, M. Chiang *et al.*, “High-resolution medical image synthesis using progressively grown generative adversarial networks,” *arXiv:1805.03144*, 2018.

[18] S. U. Dar, M. Yurt, L. Karacan, A. Erdem, E. Erdem, and T. Çukur, “Image synthesis in multi-contrast MRI with conditional generative adversarial networks,” *IEEE Trans. Med. Imag.*, vol. 38, no. 10, pp. 2375–2388, 2019.

[19] B. Yu, L. Zhou, L. Wang, J. Fripp, and P. Bourgeat, “3D cGAN based cross-modality MR image synthesis for brain tumor segmentation,” *ISBI*, pp. 626–630, 2018.

[20] B. Yu, L. Zhou, L. Wang, Y. Shi, J. Fripp, and P. Bourgeat, “Ea-gans: edge-aware generative adversarial networks for cross-modality mr image synthesis,” *IEEE Trans Med Imaging*, vol. 38, no. 7, pp. 1750–1762, 2019.

[21] D. Nie, R. Trullo, J. Lian, L. Wang, C. Petitjean, S. Ruan *et al.*, “Medical image synthesis with deep convolutional adversarial networks,” *IEEE Trans. Biomed. Eng.*, vol. 65, no. 12, pp. 2720–2730, 2018.

[22] K. Armanious, C. Jiang, M. Fischer, T. Küstner, T. Hepp, K. Nikolaou *et al.*, “MedGAN: Medical image translation using GANs,” *Comput. Med. Imaging Grap.*, vol. 79, p. 101684, 2019.

[23] D. Lee, J. Kim, W.-J. Moon, and J. C. Ye, “CollaGAN: Collaborative GAN for missing image data imputation,” in *CVPR*, 2019, pp. 2487–2496.

[24] H. Li, J. C. Paetzold, A. Sekuboyina, F. Kofler, J. Zhang, J. S. Kirschke *et al.*, “DiamondGAN: Unified multi-modal generative adversarial networks for MRI sequences synthesis,” in *MICCAI*, 2019, pp. 795–803.

[25] T. Zhou, H. Fu, G. Chen, J. Shen, and L. Shao, “Hi-Net: Hybrid-fusion network for multi-modal MR image synthesis,” *IEEE Trans. Med. Imag.*, vol. 39, no. 9, pp. 2772–2781, 2020.

[26] G. Wang, E. Gong, S. Banerjee, D. Martin, E. Tong, J. Choi *et al.*, “Synthesize high-quality multi-contrast magnetic resonance imaging from multi-echo acquisition using multi-task deep generative model,” *IEEE Trans. Med. Imag.*, vol. 39, no. 10, pp. 3089–3099, 2020.

[27] M. Yurt, S. U. Dar, A. Erdem, E. Erdem, K. K. Oguz, and T. Çukur, “mustGAN: multi-stream generative adversarial networks for MR image synthesis,” *Med. Image. Anal.*, vol. 70, p. 101944, 2021.

[28] X. Zhang, X. He, J. Guo, N. Ettehadi, N. Aw, D. Semanek *et al.*, “PTNet: A high-resolution infant MRI synthesizer based on transformer,” *arXiv:2105.13993*, 2021.

[29] Y. Korkmaz, T. Çukur, and V. M. Patel, “Self-supervised mri reconstruction with unrolled diffusion models,” in *MICCAI*, 2023, pp. 491–501.

[30] O. Oktay, J. Schlemper, L. L. Folgoc, M. J. Lee, M. Heinrich, K. Misawa *et al.*, “Attention U-Net: Learning where to look for the pancreas,” *arXiv:1804.03999*, 2018.

[31] H. Lan, A. Toga, and F. Sepehrband, “SC-GAN: 3D self-attention conditional GAN with spectral normalization for multi-modal neuroimaging synthesis,” *bioRxiv:2020.06.09.143297*, 2020.

[32] H.-C. Shin, A. Ihsani, S. Mandava, S. T. Sreenivas, C. Forster, J. Cha *et al.*, “GANBERT: Generative adversarial networks with bidirectional encoder representations from transformers for MRI to PET synthesis,” *arXiv:2008.04393*, 2020.

[33] O. Dalmaz, M. Yurt, and T. Çukur, “ResViT: Residual vision transformers for multi-modal medical image synthesis,” *IEEE Trans Med Imaging*, vol. 44, no. 10, pp. 2598–2614, 2022.

[34] J. Liu, S. Pasumarthi, B. Duffy, E. Gong, K. Datta, and G. Zaharchuk, “One Model to Synthesize Them All: Multi-Contrast Multi-Scale Transformer for Missing Data Imputation,” *IEEE Trans Med Imaging*, vol. 42, no. 9, pp. 2577–2591, 2023.

[35] J. Chen, Y. Lu, Q. Yu, X. Luo, E. Adeli, Y. Wang *et al.*, “TransUNet: Transformers make strong encoders for medical image segmentation,” *arXiv:2102.04306*, 2021.

[36] H. A. Bedel, I. Sivgin, O. Dalmaz, S. U. Dar, and T. Çukur, “Bolt: Fused window transformers for fmri time series analysis,” *Med Image Anal*, vol. 88, p. 102841, 2023.

[37] L. Zhu, B. Liao, Q. Zhang, X. Wang, W. Liu, and X. Wang, “Vision mamba: Efficient visual representation learning with bidirectional state space model,” *arXiv:2401.09417*, 2024.

[38] Y. Liu, Y. Tian, Y. Zhao, H. Yu, L. Xie, Y. Wang *et al.*, “Vmamba: Visual state space model,” *arXiv:2401.10166*, 2024.

[39] M. Heidari, S. G. Kolahi, S. Karimijafarbigloo, B. Azad, A. Bozorgpour, S. Hatami *et al.*, “Computation-efficient era: A comprehensive survey of state space models in medical image analysis,” *arXiv:2406.03430*, 2024.

[40] J. Ma, F. Li, and B. Wang, “U-mamba: Enhancing long-range dependency for biomedical image segmentation,” *arXiv:2401.04722*, 2024.

[41] Z. Xing, T. Ye, Y. Yang, G. Liu, and L. Zhu, “Segmamba: Long-range sequential modeling mamba for 3d medical image segmentation,” *arXiv:2401.13560*, 2024.

[42] J. Liu, H. Yang, H.-Y. Zhou, Y. Xi, L. Yu, Y. Yu *et al.*, “Swin-umamba: Mamba-based unet with imagenet-based pretraining,” *arXiv:2402.03302*, 2024.

[43] J. Huang, L. Yang, F. Wang, Y. Nan, A. I. Aviles-Rivero, C.-B. Schönlieb *et al.*, “MambaMR: An Arbitrary-Masked Mamba for Joint Medical Image Reconstruction and Uncertainty Estimation,” *arXiv:2402.18451*, 2024.

[44] Y. Yue and Z. Li, “Medmamba: Vision mamba for medical image classification,” *arXiv:2403.03849*, 2024.

[45] R. Xu, S. Yang, Y. Wang, Y. Cai, B. Du, and H. Chen, “Visual mamba: A survey and new outlooks,” *arXiv:2404.18861*, 2024.

[46] X. Liu, C. Zhang, and L. Zhang, “Vision mamba: A comprehensive survey and taxonomy,” *arXiv:2405.04404*, 2024.

[47] J. Zhao, D. Li, Z. Kassam, J. Howey, J. Chong, B. Chen *et al.*, “Tripartite-GAN: Synthesizing liver contrast-enhanced MRI to improve tumor detection,” *Med. Image. Anal.*, vol. 63, p. 101667, 2020.

[48] Z. Yuan, M. Jiang, Y. Wang, B. Wei, Y. Li, P. Wang *et al.*, “SARA-GAN: Self-attention and relative average discriminator based generative adversarial networks for fast compressed sensing MRI reconstruction,” *Front. Neuroinform.*, vol. 14, p. 58, 2020.

[49] F. Arslan, B. Kabas, O. Dalmaz, M. Ozbey, and T. Çukur, “Self-consistent recursive diffusion bridge for medical image translation,” *arXiv:2405.06789*, 2024.

[50] Y. Korkmaz, S. U. H. Dar, M. Yurt, M. Ozbey, and T. Cukur, “Unsupervised MRI reconstruction via zero-shot learned adversarial transformers,” *IEEE Trans Med Imaging*, vol. 41, no. 7, pp. 1747–1763, 2022.

[51] J. Ruan and S. Xiang, “VM-UNet: Vision Mamba UNet for Medical Image Segmentation,” *arXiv:2402.02491*, 2024.

[52] Z. Ju and W. Zhou, “Vm-ddpm: Vision mamba diffusion for medical image synthesis,” *arXiv:2405.05667*, 2024.

[53] K. He, X. Zhang, S. Ren, and J. Sun, “Deep residual learning for image recognition,” in *CVPR*, 2016, pp. 770–778.

[54] I. Tolstikhin, N. Houlsby, A. Kolesnikov, L. Beyer, X. Zhai, T. Unterthiner *et al.*, “Mlp-mixer: An all-mlp architecture for vision,” 2021.

[55] U. Baid, S. Ghodasara, S. Mohan, M. Bilello, E. Calabrese, E. Colak *et al.*, “The rsna-asnr-miccai brats 2021 benchmark on brain tumor segmentation and radiogenomic classification,” *arXiv:2107.02314*, 2021.

[56] T. Nyholm, S. Svensson, S. Andersson, J. Jonsson, M. Sohlin, C. Gustafsson *et al.*, “MR and CT data with multiobserver delineations of organs in the pelvic area—part of the gold atlas project,” *Med. Phys.*, vol. 45, no. 3, pp. 1295–1300, 2018.

[57] A. Sharma and G. Hamarneh, “Missing MRI pulse sequence synthesis using multi-modal generative adversarial network,” *IEEE Trans. Med. Imag.*, vol. 39, pp. 1170–1183, 2020.

[58] O. Dalmaz, M. U. Mirza, G. Elmas, M. Ozbey, S. U. Dar, E. Ceyani *et al.*, “One model to unite them all: Personalized federated learning of multi-contrast MRI synthesis,” *Med Image Anal*, vol. 94, p. 103121, 2024.

[59] J. Wolterink, A. M. Dinkla, M. Savenije, P. Seevinck, C. Berg, and I. Isgum, “Deep MR to CT synthesis using unpaired data,” in *SSMI*, 2017, pp. 14–23.

[60] M. Özbeý, S. U. Dar, H. A. Bedel, O. Dalmaz, S. Öztürk, A. Güngör *et al.*, “Unsupervised medical image translation with adversarial diffusion models,” *IEEE Trans Med Imaging*, vol. 42, no. 12, pp. 3524–3539, 2023.

[61] Y. Ge, D. Wei, Z. Xue, Q. Wang, X. Zhou, Y. Zhan *et al.*, “Unpaired MR to CT synthesis with explicit structural constrained adversarial learning,” in *ISBI*, 2019, pp. 1096–1099.

[62] B. Zhan, D. Li, Y. Wang, Z. Ma, X. Wu, J. Zhou *et al.*, “LR-cGAN: Latent representation based conditional generative adversarial network for multi-modality MRI synthesis,” *Biomed. Signal Process. Control*, vol. 66, p. 102457, 2021.

[63] D. Nie and D. Shen, “Adversarial Confidence Learning for Medical Image Segmentation and Synthesis,” *Int. J. Comput. Vision*, vol. 128, no. 10, pp. 2494–2513, 2020.

[64] A. Güngör, S. U. Dar, S. Öztürk, Y. Korkmaz, G. Elmas, M. Özbeý *et al.*, “Adaptive diffusion priors for accelerated MRI reconstruction,” *Med Image Anal*, vol. 88, p. 102872, 2023.

[65] Z. Wang, Y. Yang, Y. Chen, T. Yuan, M. Sermesant, H. Delingette *et al.*, “Mutual information guided diffusion for zero-shot cross-modality medical image translation,” *IEEE Trans Med Imaging*, pp. 1–1, 2024.

[66] M. U. Mirza, O. Dalmaz, H. A. Bedel, G. Elmas, Y. Korkmaz, A. Gungor *et al.*, “Learning Fourier-Constrained Diffusion Bridges for MRI Reconstruction,” *arXiv:2308.01096*, 2023.